Electromagnetic field fluctuation and its correlation with the participant plane in Au + Au and isobaric collisions at $\sqrt{s_{NN}} = 200$ GeV

Sk Noor Alam[*]

Department of Physics, Aligarh Muslim University, Aligarh 202002, India

Victor Roy[†]

National Institute Of Science Education and Research, HBNI, Jatni, 752050, India

Shakeel Ahmad

Department of Physics, Aligarh Muslim University, Aligarh 202002, India

Subhasis Chattopadhyay

Variable Energy Cyclotron Centre, HBNI, Kolkata, WB-700064, India

Intense transient electric (**E**) and magnetic (**B**) fields are produced in the high-energy heavy-ion collisions. The electromagnetic fields produced in such high-energy heavy-ion collisions are proposed to give rise to a multitude of exciting phenomenon including the chiral magnetic effect. We use a Monte Carlo (MC) Glauber model to calculate the electric and magnetic fields, more specifically their scalar product **E** · **B**, as a function of space-time on an event-by-event basis for the Au + Au collisions at $\sqrt{s_{NN}} = 200$ GeV for different centrality classes. We also calculate the same for the isobars ruthenium and zirconium at $\sqrt{s_{NN}} = 200$ GeV. In the QED sector, **E** · **B** acts as a source of chiral separation effect, chiral magnetic wave, etc., which are phenomena associated to the chiral magnetic effect. We also study the relationships between the electromagnetic symmetry plane angle defined by **E** · **B** ($\psi_{E.B}$) and the participant plane angle ψ_P defined from the participating nucleons for the second- to fifth-order harmonics.

I. INTRODUCTION

The initial-state fluctuations in high-energy heavy-ion collisions play an essential role in understanding several bulk observables. We can attribute the two primary sources of these initial-state fluctuations to the event-by-event geometry fluctuations of the nucleon's position inside the nuclei due to the nuclear wave function and the fluctuation in impact strong fluctuating transient electro-magemtic (EM) fields in the overlap zone of the colliding nucleus. The EM field generated in high-energy heavy-ion collision experiments such as the Relativistic Heavy Ion Collider (RHIC) and the Large Hadron Collider (LHC) is known to have the strongest magnetic field in the Universe (e.g., B ∼ 10^{18}–10^{19} Gauss for $\sqrt{s_{NN}} = 200$ GeV) [1–6].

[*]noor1989phyalam@gmail.com
[†]victor@niser.ac.in

The magnetic field in heavy-ion collisions, while averaged over many events, mostly obeys a linear scaling with the center of mass energy ($\sqrt{s}$) and the impact parameter (b) of collisions [7], i.e., $\langle eB_y \rangle \sim Zb\sqrt{s}$ for $b \leq 2R_A$, where Z is the charge number of the colliding ions and R_A is the radius of the nucleus. As per the convention, we take the y axis perpendicular to the reaction plane defined by the impact parameter (chosen along the x axis) and the beam direction (z axis). Furthermore, the event-averaged electric fields are also found to be of the same order of magnitude as the magnetic fields (e.g., $eB \approx eE \sim 10m_\pi^2$ at the topmost RHIC energy Au + Au collisions $\sqrt{s_{NN}} = 200$ GeV where m_π is the pion mass) [8].

It has been conjectured that, in addition to the standard ohmic current driven by the electric field, there might appear other new types of current in parity (P) and charge conjugation (C) odd regions in Quark-Gluon Plasma as responses to the electromagnetic fields. One of this new type of currents is generated along the background magnetic field, also known as the chiral magnetic effect (CME) [1,9–11]. In other words, in high-energy heavy-ion collisions, special gluonic configurations (sphalerons and instantons) break the P and the CP in the presence of a

strong magnetic field. It results in a global electric charge separation with respect to the reaction plane [12,13]. This charge separation occurs through the transition of the right-handed quarks to the left-handed quarks and vice versa depending on the sign of topological charges [1]. Because of their close association with axial anomaly and the topologically nontrivial vacuum structure of QCD, the CME and other associated phenomena such as the chiral separation effect (CSE) and the chiral electric separation effect are known as anomalous effects [14].

It is known that only the lowest Landau level contributes to the CME. In the QED sector, combined electric (**E**) and magnetic fields (**B**) are responsible for the transition of chiral fermions from the left-handed chirality branch to the right-handed chirality branch at a rate $\sim e^2/(2\pi^2)\mathbf{E}\cdot\mathbf{B}$ [11,14].

Similarly, in CSE, the axial current is known to be not conserved due to a source term proportional to $\sim e^3/(2\pi^2)\mathbf{E}\cdot\mathbf{B}$. The same term also appears in the chiral magnetic wave equation if $\mathbf{E}\cdot\mathbf{B}$ is nonzero. In other words, $\mathbf{E}\cdot\mathbf{B}$ pumps chirality into the system. In Ref. [15], it was shown that the current conservation equation in a relativistic fluid with one conserved charge, with a $U(1)$ anomaly, contains a source term proportional to $E^\mu B_\mu$. The scalar product of the four vectors E^μ and B^μ in the fluid rest frame is $\mathbf{E}\cdot\mathbf{B}$. Hence, it is interesting to study $\mathbf{E}\cdot\mathbf{B}$ for different collision geometry and its possible correlation with the symmetry (participant) plane, with respect to which we search for the CME signal. It is worthwhile to mention that, although the event-averaged magnetic field shows a linear behavior with the collision centrality, the electric field, on the other hand, shows an opposite trend, i.e., maximum for the central collisions and gradually decreases toward peripheral collisions. In this paper, we focus on the spatial distribution of $\mathbf{E}\cdot\mathbf{B}$ for various centrality of the Au + Au, Ru + Ru, and Zr + Zr collisions at $\sqrt{s_{NN}} = 200$ GeV to investigate the interrelation with the geometry of the fireball. To this end, we introduce the participant plane ψ_{EB} defined with the weight of $\mathbf{E}\cdot\mathbf{B}$ to investigate the relation of it with the participant plane ψ_{pp}.

The rest of this paper is organized as follows. In Sec. II, we describe the detail of calculating electromagnetic fields from the Glauber model on an event-by-event basis. We also discuss their impact parameter dependence and the event-averaged values. In Sec. III. we discuss the main results, which consist of the impact parameter, space-time, and system size dependence of $\mathbf{E}\cdot\mathbf{B}$ and its interrelation with the participant plane. Finally, we summarize this study in Sec. IV.

II. CALCULATION OF ELECTRIC AND MAGNETIC FIELD

Customarily, the electromagnetic field generated by a relativistic charged particle is calculated from the well-known Liénard-Wiechert potentials; however, we will calculate it from the second-rank antisymmetric electromagnetic field tensor $F^{\alpha\beta} = \partial^\alpha A^\beta - \partial^\beta A^\alpha$ using the Lorentz transformation. Here, A^μ is the 4-potential due to an electric charge; in the following calculations, we assume the charged protons inside the colliding nuclei move in a straight-line trajectory and there is negligible change in momentum after the collision. The calculation goes as follows [16]. First, we calculate the component of electromagnetic fields and corresponding $F'^{\gamma\delta}$ in the rest frame S' of the charge particle. The fields in the laboratory frame have been calculated from $F^{\alpha\beta}$, which is obtained from $F'^{\gamma\delta}$ through the Lorentz transformation,

$$F^{\alpha\beta} = \frac{\partial x^\alpha}{\partial x'^\gamma}\frac{\partial x^\beta}{\partial x'^\delta}F'^{\gamma\delta}, \tag{1}$$

or in matrix notation $F = \Lambda F'\tilde{\Lambda}$, where Λ is the matrix representation of the Lorentz transformation and $\tilde{x}^\mu$ corresponds to the transpose of x^μ. We choose a boost $\beta = v_z$ along the z axis. In this case, it can be easily shown that the electric fields transform as

$$E_x = \gamma E'_x + \gamma\beta B'_y, \tag{2}$$

$$E_y = \gamma E'_y - \gamma\beta B'_x, \tag{3}$$

$$E_z = E'_z \tag{4}$$

and the magnetic fields transform as

$$B_x = \gamma B'_x - \gamma\beta E'_y, \tag{5}$$

$$B_y = \gamma B'_y + \gamma\beta E'_x, \tag{6}$$

$$B_z = B'_z. \tag{7}$$

Since the charge is at rest in the S' frame $B'_x = B'_y = B'_z = 0$, furthermore, it is easy to verify $\mathbf{B} = \beta \times \mathbf{E}$. Next, we calculate $\mathbf{E}'$ at a point P (x, y, z) at time t for a charge at (x'_c, y'_c, z'_c) at time t' by noting that $z'_c \approx \beta t'$ (we assume that the origin of the laboratory frame S and the moving frame S' coincide at $t = t' = 0$). The subscript c corresponds to the charge. For convenience, we denote the transverse distance $\zeta = \sqrt{(x'_c - x)^2 + (y'_c - y)^2}$; the distance from the charge to P is $r' = \sqrt{\zeta^2 + \beta^2 t'^2}$ (here, we have taken the center of the nucleus to be at the origin of S'). Also, the positions of the charged particles in the transverse plane are assumed to be frozen due to large Lorentz $\gamma = (1 - \beta^2)^{-1/2}$. A straightforward calculation gives the values of the electric fields in the S frame,

$$E_x = \frac{\gamma q x}{(\zeta^2 + \beta^2\gamma^2(t - \beta z)^2)^{3/2}}, \tag{8}$$

$$E_y = \frac{\gamma q y}{(\zeta^2 + \beta^2 \gamma^2 (t - \beta z)^2)^{3/2}}, \tag{9}$$

$$E_z = \frac{q \beta \gamma (t - \beta z)}{(\zeta^2 + \beta^2 \gamma^2 (t - \beta z)^2)^{3/2}}, \tag{10}$$

and the magnetic fields are given by

$$B_x = \frac{-\gamma \beta q y}{(\zeta^2 + \beta^2 \gamma^2 (t - \beta z)^2)^{3/2}}, \tag{11}$$

$$B_y = \frac{\gamma \beta q x}{(\zeta^2 + \beta^2 \gamma^2 (t - \beta z)^2)^{3/2}}, \tag{12}$$

$$B_z = 0. \tag{13}$$

The total electromagnetic field at any point is evaluated using the principle of superposition, i.e., calculating fields using Eq. (8)–(13) for all the protons inside the nucleus. We use a cutoff value of $\zeta = 0.3$ fm while calculating the electric and magnetic fields using Eq. (8)–(13). This cutoff value was chosen as an average effective distance between the quarks inside the nucleons, and it was also reported [6] that there is a weak dependence of the field values on ζ in the range 0.3 to 0.6 fm. Since the colliding nucleus at $\sqrt{s_{NN}} = 200$ GeV has Lorentz $\gamma \sim 100$, we can safely assume the nucleus as a flat disk that has a vanishing thickness along the z axis. Also, due to the time dilation, the nucleons will appear as frozen inside the nucleus, and all nucleons effectively move along z with constant v_z. i.e., $\mathbf{v_n} \equiv (0, 0, v_z)$. As per the convention, we take the velocity of the target nucleus as $+v_z$, and the velocity of the projectile nucleus is $-v_z$. v_z is calculated from the ratio of the relativistic momentum and the energy of a proton

$$v_z = \sqrt{1 - \left(\frac{2m_p}{\sqrt{s_{NN}}}\right)^2}, \tag{14}$$

To obtain the nucleon positions, we use the Monte Carlo Glauber model [17]. We also calculate the initial spatial eccentricity (ϵ, defined later) and the number of participating nucleons (N_{part}) for a given impact parameter from the MC Glauber model. In the MC Glauber model, the positions of the nucleons inside the nucleus are determined by the nuclear density function measured in low-energy electron scattering experiments [18]. The functional form of this distribution is

$$\rho(r, \theta) = \frac{\rho_0}{1 + \exp\left[\frac{r - R(1 + \beta_2 Y_2^0(\theta))}{a}\right]}, \tag{15}$$

where ρ_0 corresponds to the nuclear density at the center, R is the radius of the nucleus, and a is the skin depth (it controls how quickly the nuclear density falls off near the edge of the nucleus). The spherical harmonics $Y_l^m(\theta)$ and

parameter β_2 are used to measure the deformation from spherical shape. For our study, we take $R = 6.38$ fm, $a = 0.535$ fm, and $\beta_2 = 0$ for the Au_{79}^{197} nucleus. We use parameter $\beta_2^{Ru} = 0.158$, $\beta_2^{Zr} = 0.08$, $R^{Ru} = 5.085$ fm, $R^{Zr} = 5.02$ fm, and $a = 0.46$ fm for both Ru and Zr [19–21].

We sample the nucleon positions, assuming that they are randomly distributed with the given distribution $4\pi r^2 \rho(r)$ (integrating on θ and ϕ) for the Au nucleus and $r^2 \sin(\theta) \rho(r, \theta)$ for Ru and Zr nuclei, respectively.

The impact parameters b of the collisions are randomly selected from the distribution $\frac{dN}{db} \sim b$ up to a maximum value of $\simeq 20$ fm $> 2R$. The center of the target and projectile nuclei are shifted to $(-\frac{b}{2}, 0, 0)$ and $(\frac{b}{2}, 0, 0)$, respectively. We use the inelastic nucleon-nucleon cross section $\sigma_{NN} = 42$ mb for the top RHIC energy $\sqrt{s_{NN}} = 200$ GeV for calculating the probability of an interaction between the target and the projectile nucleons [22,23]. To show the centrality dependence, we calculate the centrality of the collisions using N_{part} and the number of binary collisions (N_{coll}) obtained from the MC Glauber model. The multiplicity for a given N_{part} and (N_{coll}) is calculated using the two-component model as

$$\frac{dN_{ch}}{d\eta} = n_{pp}\left[(1 - x)\frac{N_{part}}{2} + x N_{coll}\right], \tag{16}$$

where x is the fraction of hard scattering and n_{pp} is the average multiplicity per unit pseudorapidity in pp collisions. The above two-component model of the particle production is based on the assumption that the average particles produced through the soft interactions are proportional to the N_{part}, and the probability of hard interactions is proportional to N_{coll}. We calculate the centrality of a given collision in the following way: the number of independent particle emitting sources for a given impact parameter is $(1 - x)\frac{N_{part}}{2} + x N_{coll}$. Each of these sources produces particles following a negative binomial distribution (NBD) with a mean μ and the width $\sim 1/k$,

$$P_{\mu,k}(n) = \frac{\Gamma(n + k)}{\Gamma(n + 1)\Gamma(k)}\left(\frac{\mu}{\mu + k}\right)^n \left(\frac{k}{\mu + k}\right)^k, \tag{17}$$

$P_{\mu,k}(n)$ is the probability of measuring n hits per independent sources. The mean of this NBD distribution is calculated from the pseudorapidity density of the charged multiplicity for the nonsingle diffractive $\bar{p}p$ collisions at a given $\sqrt{s_{NN}}$ energy [24],

$$\mu = \mathcal{A}\ln^2(s_{NN}) - \mathcal{B}\ln(s_{NN}) + \mathcal{C}, \tag{18}$$

where $\mathcal{A} = 0.023 \pm 0.008$, $\mathcal{B} = 0.25 \pm 0.19$, and $\mathcal{C} = 2.5 \pm 1.0$. The charged particle multiplicity data for Au + Au 200 GeV collisions measured by the STAR
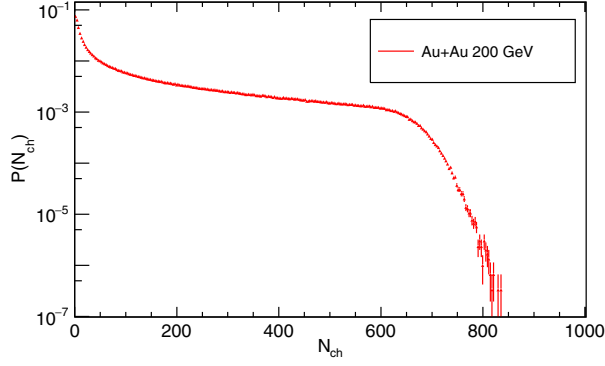
FIG. 1.   Probability distribution of the charged particles multiplicity in Au + Au $\sqrt{s_{NN}} = 200$ GeV collisions.

Collaboration are explained for $x = 0.13$ and $k = 1.7$, and $\mu = 2.08$ for the pseudorapidity range i.e., $|\eta| < 0.5$ [25]. For example, we show the charged particle multiplicity distribution for Au + Au collisions at $\sqrt{s_{NN}} = 200$ GeV for $|\eta| < 0.5$ in Fig. 1. To calculate the centrality of collisions, we subdivide the total area in Fig. 1 into different bins with the condition that the fractional area corresponds to a particular centrality. For example, the bin boundaries $n40$ and $n50$ for the 40%–50% centrality are defined in such a way that the following relation holds: $\frac{\int_{\infty}^{n40} P(N_{ch})dN_{ch}}{\int_{\infty}^{0} P(N_{ch})dN_{ch}} = 0.4$, and $\frac{\int_{\infty}^{n50} P(N_{ch})dN_{ch}}{\int_{\infty}^{0} P(N_{ch})dN_{ch}} = 0.5$. We use three centrality bins 0%–5%, 40%–50%, and 70%–80% for our calculation of the electric and magnetic fields; corresponding impact parameter ranges are 0–3.2, 9.3–10.6, and 12.2–13.5 fm, which are very similar to the values given in Ref. [25].

As mentioned earlier, the topology of the electromagnetic fields in heavy-ion collisions has nontrivial dependence on the centrality (possibly also on the $\sqrt{s_{NN}}$). Consequently, the source ($\mathbf{E} \cdot \mathbf{B}$) of the chiral current in the transverse plane also has a nontrivial centrality dependence. The axial current generated by the magnetic field is supposed to predominantly flow along the direction

perpendicular the participant plane. Hence, we investigate here how the sources $\mathbf{E} \cdot \mathbf{B}$ of this current are correlated to the participant plane. From the perspective of heavy-ion collisions, it is customary to use the Milne coordinates, i.e., we use the longitudinal proper time $\tau = \sqrt{t^2 - z^2}$, x, y, and the space-time rapidity $\eta = \frac{1}{2}\log(\frac{t+z}{t-z})$ instead of the Cartesian coordinate. We use Milne coordinates only for Fig. 2. In Fig. 2, we show the distribution of $\mathbf{E} \cdot \mathbf{B}$ for 40%–50% centrality with η (left plot) and τ (right plot). In the left plot, we calculate $\mathbf{E} \cdot \mathbf{B}$ in the forward light cone spanned by the region for $\tau = 0.4$ and $-1.0 \leq \eta \leq 1.0$. In the right plot, we also calculate $\mathbf{E} \cdot \mathbf{B}$ in the forward light cone. But for this plot, the phase space is spanned by the region for $\eta = 0.4$ and $0.1 \leq \tau \leq 0.34$. While calculating the dot product, we transform the field components $B_{x(y)}$ from the Cartesian to the Milne coordinate $\tilde{B}_{x(y)}$ by the following expressions: $\tilde{B}_x = B_x / \cosh \eta$, $\tilde{B}_y = B_y / \cosh \eta$, and $\tilde{B}_z = B_z / \tau$. The components of the electric field transform accordingly.

To investigate the distribution of $\mathbf{E} \cdot \mathbf{B}$ (from now on denoted as $\mathcal{E}$) to the participant plane, we introduce the $\mathbf{E} \cdot \mathbf{B}$ symmetry plane $\psi_{\mathcal{E}}$ defined as [26,27]

$$\epsilon_n e^{in\psi_{\mathcal{E}}} = -\frac{\int dx dy r^n e^{in\varphi} \mathcal{E}(x, y)}{\int dx dy r^n \mathcal{E}(x, y)}, \qquad (19)$$

where $r^2 = (x - \langle x \rangle)^2 + (y - \langle y \rangle)^2$ and $\tan(\varphi) = \frac{y - \langle y \rangle}{x - \langle x \rangle}$. Here, $(\langle x \rangle, \langle y \rangle)$ corresponds to the mean position of the participating nucleons. Using these definitions and Eq. (19), we obtain $\psi_{\mathcal{E}}$ as

$$\psi_{\mathcal{E}} = \frac{1}{n} \arctan \frac{\int dx dy r^n \sin(n\varphi) \mathcal{E}(x, y)}{\int dx dy r^n \cos(n\varphi) \mathcal{E}(x, y)} + \frac{\pi}{n}, \qquad (20)$$

Before going into the main results of this paper, let us very briefly go through the impact parameter dependence of the electric and magnetic fields produced in Au + Au collisions at $\sqrt{s_{NN}} = 200$ GeV. These results are not new and
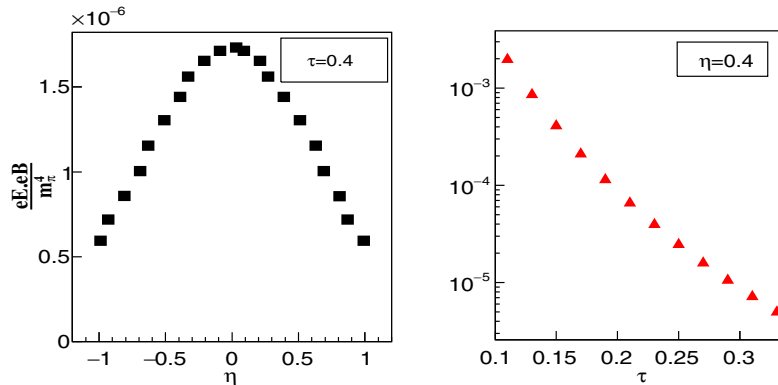

FIG. 2.   Left panel: event-averaged distribution of $\mathbf{E} \cdot \mathbf{B}$ for 40%–50% centrality Au + Au collisions at $\sqrt{s_{NN}} = 200$ GeV as a function of η at constant proper time $\tau = 0.4$. Rght panel: same as the left panel but as a function of τ at constant $\eta = 0.4$.

have already been reported in several works [6,7,14,28], but we include them for the sake of completeness.

A. Impact parameter dependence of the field

We calculate fields on a regular space-time grid and consider one million events while calculating event-averaged quantities. The magnitude of the electric and magnetic fields may become very large near the charges due to the obvious r dependence of Coulomb law, relativistic enhancement of field, and the clustering of charges due to the quantum fluctuations of the nuclear wave function [29]. But these fluctuations smooth out when taking the event average of the field due to its vector nature. These fluctuations might play an essential role in CME; however, here, we show the event-averaged values of electromagnetic fields as a function of the impact parameter of the collisions. The impact parameter dependence of electric and magnetic fields at the origin (i.e., $x = 0$, $y = 0$ in our grid space) at $t = 0$ is shown in Fig. 3. Because of the symmetry in the system considered here, $\langle E_x \rangle$ and $\langle E_y \rangle$ are zero at the origin. It is also interesting to note that $\langle |E_x| \rangle \approx \langle |E_y| \rangle \approx \langle |B_x| \rangle$ (Fig. 3). From these two figures, we also
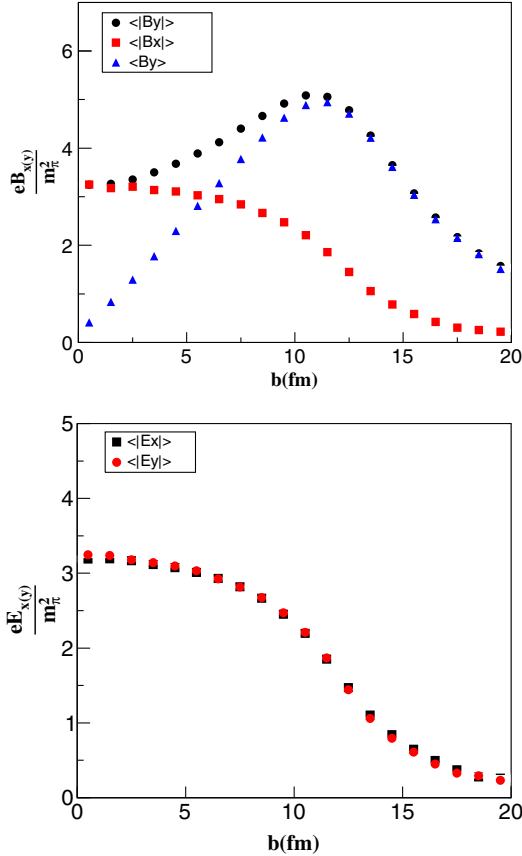
notice that the electric field decreases as the impact parameter increases, while the magnetic field follows the opposite trend. Our results seems to be consistent with Refs. [6,7].

We end this section with this brief discussion; let us turn to the quantity of our interest in the next section.

III. RESULTS AND DISCUSSION

A. impact parameter dependence of E · B

In Fig. 4, we show a one-dimensional histogram of $\mathcal{E}(0, 0)$ distribution for $z = t = 0$ and for three different centralities 0%–5% (black circles), 40%–50% (red triangles), and 70%–80% (open blue circles) Au + Au collisions at $\sqrt{s_{NN}} = 200$ GeV. First, we note that there is a nonmonotonic dependence of $\mathcal{E}$ on the collision centrality. For peripheral collisions, maximum events have $\mathcal{E} \sim 0$, and the distribution also becomes narrower compared to the central/midcentral collisions. This behavior can be understood as a consequence of near vanishing electric fields at the center of the collision zone in peripheral collisions at $t = 0$ and at midrapidity. It is clear from top panel of Fig. 4 that, although the mean of $\mathcal{E}$ (at the origin) is zero, the

FIG. 3. Top panel: event-averaged absolute value of B_x and B_y (in unit of m_π^2) at $\mathbf{r} = 0$ and t = 0 vs impact parameter for Au + Au collisions at $\sqrt{s_{NN}} = 200$ GeV. Bottom panel: same as top panel but for the electric fields.
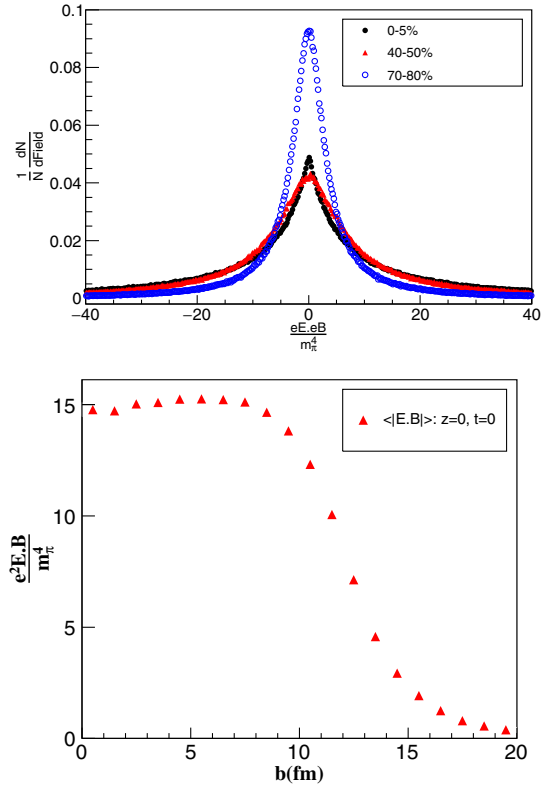

FIG. 4. Top panel: histogram of $\mathbf{E} \cdot \mathbf{B}$ at $\mathbf{r} = 0$ and $t = 0$ for 0%–5%, 40%–50%, and 70%–80% centrality of Au + Au collisions at $\sqrt{s_{NN}} = 200$ GeV. Bottom panel: event-averaged absolute value of $\mathbf{E} \cdot \mathbf{B}$ at $x = y = z = 0$ and t = 0 fm as a function of the impact parameter for Au + Au collisions at $\sqrt{s_{NN}} = 200$ GeV.
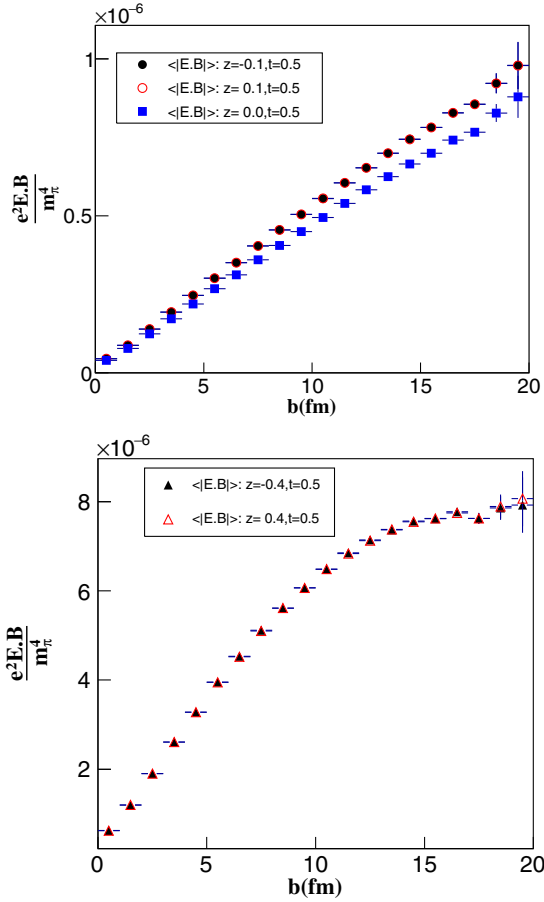
FIG. 5. Event-averaged absolute values of $\mathbf{E} \cdot \mathbf{B}$ at $x = y = 0$ for $|z| = 0.1, z = 0$ (top panel) and $|z| = 0.4$ fm (bottom panel) with the impact parameter for Au + Au collisions at $\sqrt{s_{NN}} = 200$ GeV. All results are for $t = 0.5$ fm.

variance is nonzero. Hence, it is more relevant to study the absolute value of the event averaged $\mathcal{E}$. In the bottom panel of Fig. 4 and in both panels of Fig. 5, we show the event-averaged absolute values of $\mathcal{E}(0,0)$ for $t = z = 0$ fm and $t = 0.5$ fm, $z = \pm 0.1$, and $z = \pm 0.4$, respectively. The important difference between these two results is that for the first case ($t = z = 0$ fm) electromagnetic fields from the two colliding nuclei almost equally contributed in $\mathcal{E}$, whereas, for the other case, the fields due to each nucleus will be significant for $|z| \sim t$ and are dominated by the nearest nucleus. From the bottom panel of Fig. 4, we observe that for $t = z = 0$ fm $\mathcal{E}$ is almost flat up to impact parameter $b \sim 10$ fm, and after that, it falls rapidly. This observed impact parameter dependence of $\mathcal{E}$ can be attributed to the fact that the magnetic field increases with impact parameter, whereas electric fields diminish. The magnitude of $\mathcal{E}$ (expressed in the unit of pion mass) is comparable to the corresponding magnetic fields in central collisions. It may be an overoptimistic claim at this stage; however, these large values of $\mathcal{E}$ at midrapidity at the initial time possibly indicates that the CME signal may have a significant contribution from

$\mathcal{E}$ along with B. To get the complete picture, we must wait for the late-time behavior of $\mathcal{E}$ discussed next. For the other case, we consider fields at later time $t = 0.5$ fm and at forward and backward regions, i.e., $z \neq 0$. The top panel of Fig. 5 shows the dependence of $\mathcal{E}$ as a function of b for $z = 0$ (blue squares) and $z = \pm 0.1$ (open and filled circles). It is not surprising that $\mathcal{E}$ for this case is approximately 6 orders of magnitude smaller than the $t = z = 0$ case; this is because the electromagnetic fields decay rapidly after the collision, and in this case, only one nucleus significantly contributes to the fields.

From the top panel of Fig. 5, we also observe that $\mathcal{E}$ increases almost linearly with the impact parameter; this is almost opposite of what we observe for $t = z = 0$. The impact parameter dependence of $\mathcal{E}$ at finite z is, however, nontrivial, as can be seen from the bottom panel of Fig. 5, in which the same result is shown but for $z = \pm 0.4$. Here, one notices that $\mathcal{E}$ rises almost linearly for small b (< 10 fm), but after that, it starts saturating. Since $z = \pm 0.4$ at time 0.5 fm is nearer to the receding nuclei, we get a larger value of $\mathcal{E}$ compared to $z = 0$, and $z = \pm 0.1$ (top panel). To conclude this section, we note that at peripheral collisions charge separation is experimentally observed to be larger than central collisions [30,31], and it might be linked to the observed b dependence $\mathcal{E}$, along with the magnetic fields, which are also most prominent in midcentral/peripheral collisions.

B. E · B correlation with participant plane

In Ref. [8], the correlation of the fluctuating magnetic field with the participant plane showed that a sizable suppression of the angular correlations exists between the magnetic field and the second and fourth harmonic participant planes in very central and very peripheral collisions. The importance of space averaged $e^2 \mathbf{E} \cdot \mathbf{B}$ was studied recently in Ref. [32] as a function of time for 200 GeV Au + Au collisions at $t = 0.08$ fm and for $b = 9$ fm. We notice that our finding of the spatial distribution of $\mathcal{E}$ in Au + Au collisions is similar to that in Ref. [32]. In this section, we further investigate the spatial distribution $\mathcal{E}$ and its correlation with the participant plane ψ_p by calculating the symmetry plane defined in Eq. (20). ψ_p is calculated from Eq. (20) using the positions of wounded nucleons and by setting $\mathcal{E} = 1$, which gives the usual definition used in the literature.

Since the isobaric collisions of Ru + Ru and Zr + Zr are important for searching the CME signal, we include results for these two nuclei along with the Au + Au collisions discussed in the previous section.

Let us first discuss the results for the Au + Au collisions. We show the distribution of $\psi_{\mathcal{E}}$ and ψ_P at $z = 0$ for time $t = 0$ fm in Fig. 6 for perfectly head-on ($b = 0$ fm) Au + Au collisions at $\sqrt{s_{NN}} = 200$ GeV. Since a head-on collision creates an almost symmetric overlap zone, the existence of a particular symmetry plane due to the
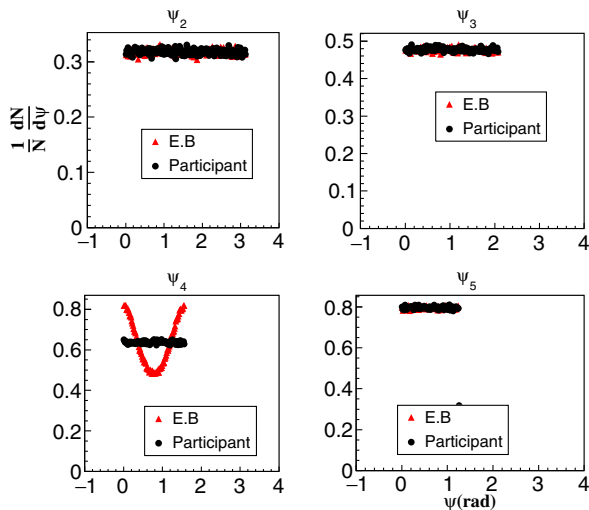
FIG. 6. Distribution of $\psi_{\mathcal{E}}^n$ and ψ_P^n ($n = 2$-5) for impact parameter $b = 0$ fm Au + Au collisions at $\sqrt{s_{NN}} = 200$ GeV.

FIG. 8. Distribution of $\psi_{\mathcal{E}}^n$ and ψ_P^n ($n = 2$-5) for 40%–50% centrality Au + Au collisions at $\sqrt{s_{NN}} = 200$ GeV.

participants (ψ_p) may be ruled out in this case. That is what we observe here from Fig. 6, in which black circles show ψ_P^2; the distribution is almost flat. The distribution of $\psi_{\mathcal{E}}^2$ is also similar to ψ_P^2; the third- and fifth-order symmetry plane show a similar trend. Interestingly, the rotational symmetry in head-on collisions seems to be broken for $\psi_{\mathcal{E}}^4$. The reason behind this behavior, however, is unclear to us. We know that the probability of occurrence of a perfectly head-on collision is approximately zero. Hence, next in Fig. 7, we show results for 0%–5% centrality Au + Au collisions at $t = z = 0$ fm.

As expected, in contrast to the $b = 0$ case, in Fig. 7, we see that, due to the overlap geometry and the fluctuating nucleon positions, the distribution of the second-order participant plane (black circles) reflects the broken
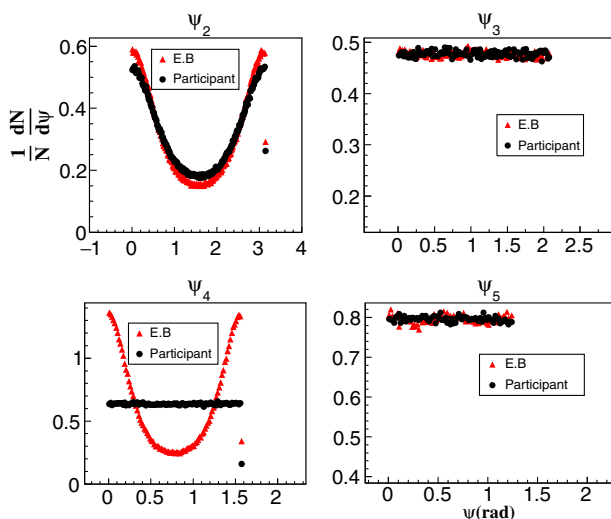

FIG. 7. Distribution of $\psi_{\mathcal{E}}^n$ and ψ_P^n ($n = 2$-5) for 0%–5% centrality Au + Au collisions at $\sqrt{s_{NN}} = 200$ GeV.
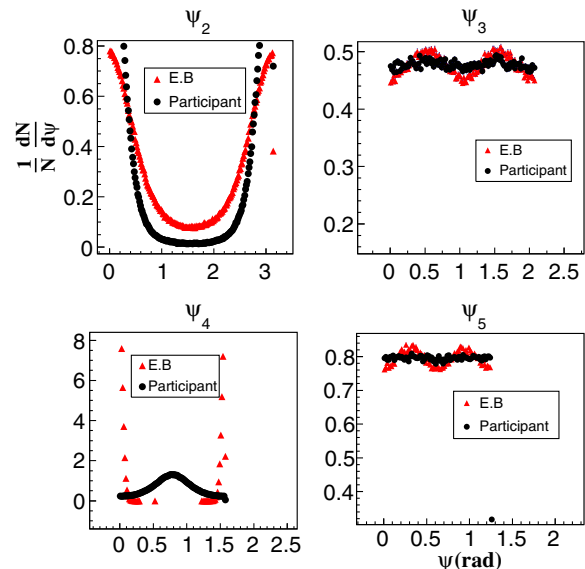
rotational symmetry of the collision zone. $\psi_{\mathcal{E}}^2$ (red triangles) due to the electromagnetic fields seems to be highly correlated with ψ_P^2. Other higher-order ψ_P's in central collisions are known to be fluctuating widely, and the same is observed here as well. Notably, $\psi_{\mathcal{E}}^4$ shows a different trend than ψ_P^4. This is because in central collisions inside the fireball the resultant electric fields due to the target and the projectile are much smaller than the magnetic fields; the magnetic fields have a dipole nature, and the corresponding symmetry plane almost coincides with ψ_P^2. This can be more clearly seen from Fig. 8 for 40%–50% centrality collisions, where the electric fields become vanishingly small and the magnetic fields are larger; in that case, $\psi_{\mathcal{E}}^4$ (bottom panel) becomes more oriented along ψ_P^2 (top panel). If we further increase the collision centrality and consider 70%–80% collisions (see Fig. 9), we observe a noticeable change in $\psi_{\mathcal{E}}^2$ as compared to the midcentral collisions. It is clear that the distribution of $\mathcal{E}$ has a $\pi/2$ rotation compared to the central collisions. To better understand this rotation of symmetry plane for peripheral collisions, we show the contours of $\mathcal{E}$ in the transverse plane for the 40%–50% (top panel) and 70%–80% (bottom panel) centralities at $z = 0$ and $t = 0$ fm in Fig. 10. We can see that a quadrupole like structure appears for 70%–80% collisions. From the above discussion, we can conclude that $\mathcal{E}$ distribution in the transverse plane for Au + Au collisions at 200 GeV per nucleon is highly correlated with the geometry of the fireball.

Ruthenium and zirconium nuclei carry the same number of nucleons (96), but Ru has 44 protons, and Zr has 40 protons. In other words, they have similar shapes and sizes but different electrical charges, which implies different electromagnetic fields generated in Ru + Ru and Zr + Zr
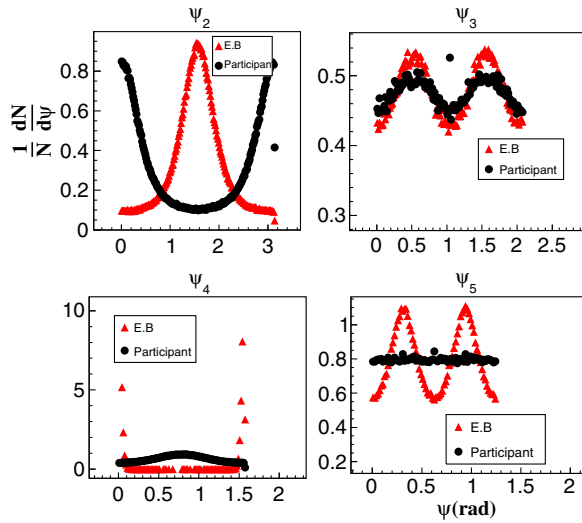
FIG. 9. Distribution of $\psi_{\mathcal{E}}^n$ and ψ_P^n (n = 2-5) for 70%–80% centrality Au + Au collisions at $\sqrt{s_{NN}}$ = 200 GeV.
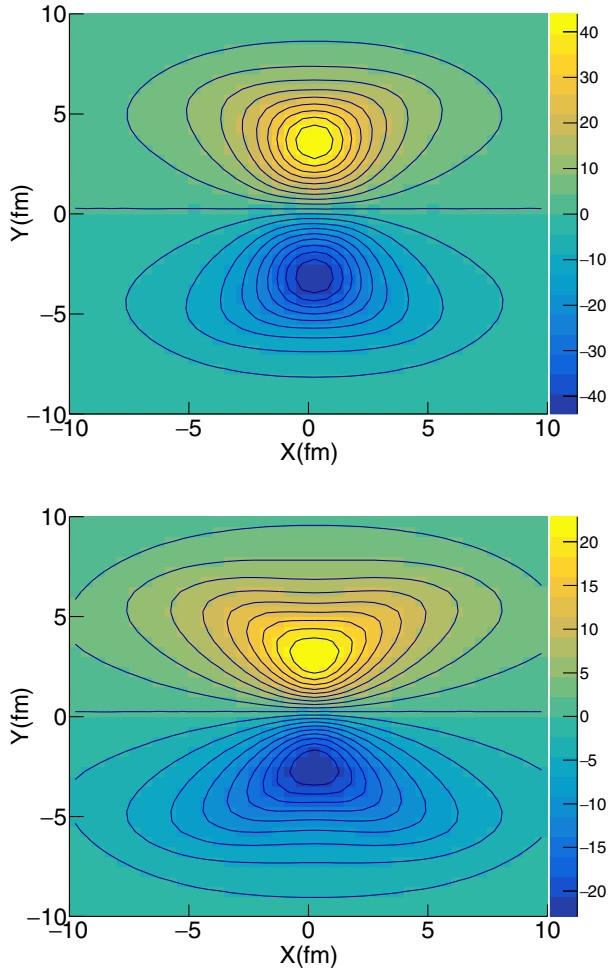

FIG. 10. Top panel: spatial distribution of $\mathcal{E}$ at $z = t = 0$ for 40%–50% centrality Au + Au collisions at $\sqrt{s_{NN}}$ = 200 GeV. Bottom panel: same as the top panel but for 70%–80% centrality.

collisions. This feature makes them interesting systems for detecting CME by eliminating possible backgrounds. For the following results, we use fixed impact parameter collisions to keep things simple.

We checked that for $b = 0$ Ru + Ru and Zr + Zr collisions (not shown here), results are very similar to what was observed for Au + Au collisions. In the top panel of Fig. 11, we show $\psi_{\mathcal{E}}^i$ and ψ_P^i ($i = 2$–5) distribution for Ru + Ru collisions at $\sqrt{s_{NN}}$ = 200 GeV for $b = 5$ fm. The bottom panel of the same figure corresponds to results for $b = 10$ fm collisions. A similar result was obtained (not shown here) for the Zr + Zr collisions. It is interesting to note that $\psi_{\mathcal{E}}$'s and ψ_P's in these small collision systems show a similar correlation as was observed for the Au + Au collisions. Like peripheral Au + Au collisions, we also
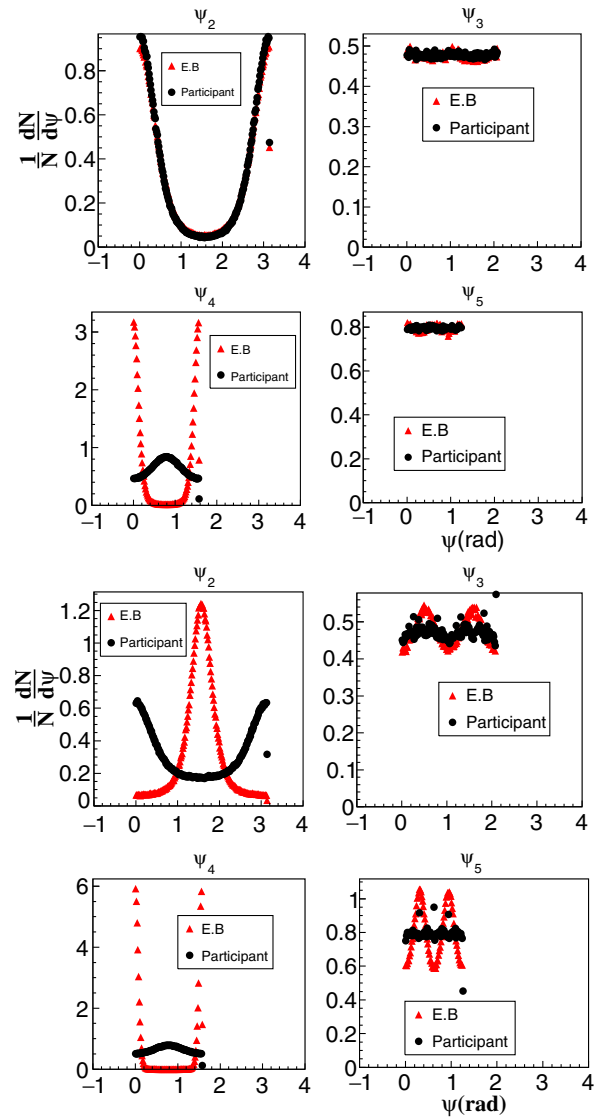

FIG. 11. Top panel: distribution of $\psi_{\mathcal{E}}$ and ψ_P for Ru + Ru collisions at $\sqrt{s_{NN}}$ = 200 GeV for $b = 5$ fm. Bottom panel: same as above but for impact parameter $b = 10$ fm.
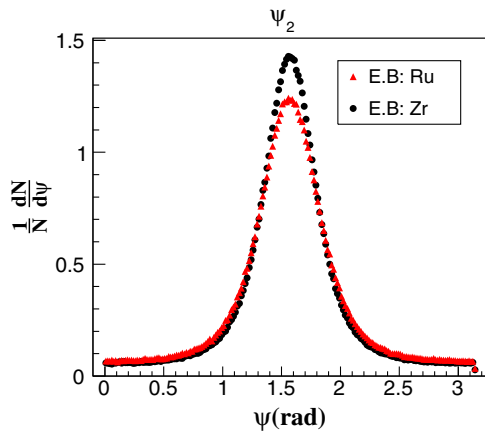
FIG. 12.   Distribution of the second-order plane $\psi_{\mathcal{E}}^2$ for Ru + Ru and Zr + Zr collisions at $\sqrt{s_{NN}} = 200$ GeV for $b = 10$ fm.

observe the rotation of $\psi_{\mathcal{E}}$ by $\pi/2$ for the peripheral Ru + Ru and Zr + Zr collisions. Because the electromagnetic field produced in Ru + Ru and Zr + Zr collisions differs, we compared $\psi_{\mathcal{E}}^2$ distribution for $b = 0$ fm. This fact is shown in Fig. 12, the field is higher for Zr + Zr compared to Ru + Ru, and possibly as a consequence, we observe a slightly narrow peak for the Zr + Zr (black dots).

IV. CONCLUSIONS

In summary, we have studied the event-by-event fluctuations of the electric and the magnetic fields and their possible correlation with the geometry of the high-energy heavy-ion collisions. More particularly, we studied the distribution of $\mathbf{E} \cdot \mathbf{B}(= \mathcal{E})$ in the transverse plane for Au + Au, Ru + Ru, and Zr + Zr collisions at $\sqrt{s_{NN}} = 200$ GeV. Further, we show the τ and η dependence of $\mathcal{E}$ in Au + Au at 200 GeV per nucleon collisions. As expected, $\mathcal{E}$ is found to be symmetric in η (around $\eta = 0$), and $\mathcal{E}$ quickly decays as a function of τ at a given η. Because $\mathcal{E}$ may contribute to CME as a source of the anomalous current, we investigate the centrality (impact parameter) dependence of the symmetry plane angle $\psi_{\mathcal{E}}$ and its possible correlation with the participant plane. We show that $\psi_{\mathcal{E}}$ is strongly correlated with ψ_P for third- and fifth-order harmonics for Au + Au, Ru + Ru, and Zr + Zr collisions. The second-order planes $\psi_{\mathcal{E}}$ and ψ_P mostly coincide with each other except for the peripheral collisions, where a rotation by $\pi/2$ is observed for $\psi_{\mathcal{E}}$, irrespective of the collision system size. This phenomenon seems to be happening due to the almost cancellation of electric fields and dominating magnetic field pointing perpendicular to the participant plane in peripheral collisions. To conclude, in this exploratory study, we show that, like the magnetic fields, $\mathcal{E}$ is also correlated to the geometry of the collision even when we consider event-by-event fluctuation of nucleon positions. Here, some comments are in order. In the present study, we have neglected the fact that the participating nucleons lose their rapidity and may have noticeable effects on the total electromagnetic fields. This contribution, although very small at midrapidity for Au + Au collisions at $\sqrt{s_{NN}} = 200$ GeV (on average, the rapidity loss is $\sim$2%–6% at midrapidity [1]), may become significant for lower-energy collisions. Also, the assumption that the nuclei have vanishing thickness along the beam direction needs to be modified for lower collision energies. We will address these topics elsewhere.

[1] D. E. Kharzeev, L. D. McLerran, and H. J. Warringa, Nucl. Phys. **A803,** 227 (2008).

[2] V. Skokov, A. Y. Illarionov, and V. Toneev, Int. J. Mod. Phys. A **24,** 5925 (2009).

[3] M. Asakawa, A. Majumder, and B. Muller, Phys. Rev. C **81,** 064912 (2010).

[4] V. Voronyuk, V. D. Toneev, W. Cassing, E. L. Bratkovskaya, V. P. Konchakovski, and S. A. Voloshin, Phys. Rev. C **83,** 054911 (2011).

[5] L. Ou and B. A. Li, Phys. Rev. C **84,** 064605 (2011).

[6] A. Bzdak and V. Skokov, Phys. Lett. B **710,** 171 (2012).

[7] W. T. Deng and X. G. Huang, Phys. Rev. C **85,** 044907 (2012).

[8] J. Bloczynskia, X.-G. Huanga, X. Zhanga, and J. Liaoa, Phys. Lett. B **718,** 1529 (2013).

[9] A. A. Belavin, A. M. Polyakov, A. S. Schwartz, and Yu. S. Tyupkin, Phys. Lett. **59B,** 85 (1975).

[10] G. Hooft, Phys. Rev. Lett. **37,** 8 (1976); Phys. Rev. D **14,** 3432 (1976).

[11] K. Fukushima, D. E. Kharzeev, and H. J. Warringa, Phys. Rev. D **78,** 074033 (2008).

[12] D. Kharzeev, Phys. Lett. B **633,** 260 (2006).

[13] S. N. Alam and S. Chattopadhyay, Nucl. Phys. **A977,** 208 (2018).

[14] X. G. Huang, Rep. Prog. Phys. **79,** 076302 (2016).

[15] D. T. Son and P. Surowka, Phys. Rev. Lett. **103,** 191601 (2009).

[16] J. D Jackson, *Classical Electrodynamics*, 3rd ed. (John Wiley & Sons, Inc, 2007)

[17] M. L. Miller, K. Reygers, S. J. Sanders, and P. Steinberg, Annu. Rev. Nucl. Part. Sci. **57**, 205 (2007).

[18] H. De Vries, C. W. De Jager, and C. De Vries, At. Data Nucl. Data Tables **36**, 495 (1987).

[19] S. Raman, C. W. G. Nestor, Jr., and P. Tikkanen, At. Data Nucl. Data Tables **78**, 1 (2001).

[20] B. Pritychenko, M. Birch, B. Singh, and M. Horoi, At. Data Nucl. Data Tables **107**, 1 (2016).

[21] P. Moller, J. R. Nix, W. D. Myers, and W. J. Swiatecki, At. Data Nucl. Data Tables **59**, 185 (1995).

[22] See, https://twiki.cern.ch/twiki/bin/view/Main/LHCGlauber Baseline.

[23] Y. M. Yao *et al.*, J. Phys. G **33**, 1 (2006).

[24] F. Abeet *et al.* (CDF Collaboration), Phys. Rev. D **41**, 2330 (1990).

[25] B. I. Abelev *et al.* (STAR Collaboration), Phys. Rev. C **79**, 034909 (2009).

[26] B. Alver and G. Roland, Phys. Rev. C **81**, 054905 (2010).

[27] B. H. Alver, C. Gombeaud, M. Luzum, and J. Y. Ollitrault, Phys. Rev. C **82**, 034913 (2010).

[28] X.-L. Zhao, G.-L. Ma, and Y.-G. Ma, Phys. Rev. C **99**, 034903 (2019).

[29] V. Roy and S. Pu Phys. Rev. C **92**, 064902 (2015).

[30] B. I. Abelev *et al.* (STAR Collaboration), Phys. Rev. Lett. **103**, 251601 (2009).

[31] B. Abelev *et al.* (ALICE Collaboration), Phys. Rev. Lett. **110**, 012301 (2013).

[32] I. Siddique, X.-L. Sheng, and Q. Wang, Phys. Rev. C **104**, 034907 (2021).